

# Eddy Loss Analysis and Parameter Optimization of the WPT System in Seawater

Ke-Han Zhang<sup>\*</sup>, Zheng-Biao Zhu<sup>†</sup>, Luo-Na Du<sup>\*</sup>, and Bao-Wei Song<sup>\*</sup>

<sup>†,\*</sup>School of Marine Science and Technology, Northwestern Polytechnical University, Xi'an, China

## Abstract

Magnetic resonance wireless power transfer (WPT) in the marine environment can be utilized in many applications. However, energy loss in seawater through eddy loss (EL) is another consideration other than WPT in air. Therefore, the effect of system parameters on electric field intensity (EFI) needs to be measured and ELs calculated to optimize such a system. In this paper, the usually complicated analytical expression of EFI is simplified to the product of frequency, current, coil turns, and a coefficient to analyze the eddy current loss (ECL). Moreover, as the calculation of ECL through volume integral is time-consuming, the equivalent eddy loss impedance (EELI) is proposed to help designers determine the optimum parameters quickly. Then, a power distribution model in seawater is conceived based on the introduction of EELI. An optimization flow chart is also proposed according to this power distribution model, from which a prototype system is developed which can deliver 100 W at 90% efficiency with a gap of 30 mm and a frequency of 107.1 kHz.

**Key words:** Eddy loss, Equivalent eddy loss impedance, Power distribution model

## I. INTRODUCTION

The application of wireless power transfer (WPT) technology to charge submersible vehicles has potential economic and operational benefits over the complicated and expensive submerged wet-mate connector technology used for wired power transfer in seawater [1]-[3]. Most of the research and development of WPT technology has focused on atmospheric environments [4], [5], while studies in submersed conditions remain in the early stages. Kojiya et al. schematized a flow chart for designing coils and a cone-style coil was designed for inductive power transfer (IPT), which achieved the transfer of 1 kW of power in seawater [6]. Baer et al. designed a connector that could transfer power through IPT and data through optical windows [7]. An antenna designed by Fukuda et al. transferred power using low resonance frequency with 40% efficiency and signal data at a higher frequency with a transmission rate of 20 Mbps [8]. Tibajia and Talampas conducted experiments in air, water, and seawater to investigate the influence of seawater on

power transfer and bit error rate (BER) [9]. Ogihara analyzed power transmission efficiency variation with frequency and transmission gap and designed a hardware capable of transferring power with approximately 81% efficiency and data with 0.1% BER within 30 mm [10]. Bana et al. presented a WPT system design for underwater applications and demonstrated that transferring power between water and air has only a slight difference when the frequency is below 250 kHz [11]. Cheng proposed a novel semi-closed magnetic core structure of an underwater loosely coupled transformer [12] that can improve the coupling coefficient and reduce electromagnetic radiation. Guidelines based on theoretical calculations of electric field intensity (EFI) are provided to select the optimum frequency for maximizing efficiency [13].

The literature aforementioned, while of significant value in the application of WPT technology in seawater, leaves some remaining issues unsolved. As the conductivity of air at standard temperature and pressure is effectively zero, the mutual inductance model [14]-[16] giving the relationship of the primary side current and the secondary side inductive voltage does not incorporate the medium loss. Therefore, applying the mutual model directly into a WPT system in seawater is erroneous. The eddy loss (EL) caused by seawater has a significant influence on transfer efficiency because the resonance frequency of the magnetic resonance WPT system

Manuscript received Sep. 21, 2017; accepted Jan. 30, 2018

Recommended for publication by Associate Editor M. Vilathgamuwa.

<sup>†</sup>Corresponding Author: 1016872417@qq.com

Tel: +86-18702947889, Northwestern Polytechnical University

<sup>\*</sup>Sch. of Marine Sci. and Tech., Northwestern Polytechnical Univ., China

is usually above 100 kHz. To elucidate the influence of EL on the WPT system, the EFI excited by circular current is measured, EL is calculated, and the equivalent eddy loss impedance (EELI) is then added into the circuit model of the WPT system. A power distribution model is proposed that forms the foundation for optimizing the WPT system in seawater. Although the WPT system can be optimized by experimentation, it is too time-consuming because the coil turns or resonance frequency needs to be changed many times until the optimum parameters are found. Additionally, optimization by calculation is a monumental task if the numerical method proposed in [13] is adopted. Therefore, a fast way to calculate EELI is proposed that accelerates the process of optimum parameters.

## II. WPT SYSTEM IN AIR

The basic circuit model of a WPT system is shown in Fig. 1.  $R_{\text{coil}_P}$  and  $R_{\text{coil}_S}$  represent the coil resistances of Coil<sub>Tx</sub> and Coil<sub>Rx</sub>.  $L_P$  and  $L_S$  are the self-inductances of Coil<sub>Tx</sub> and Coil<sub>Rx</sub>.  $R_L$  is the load.  $C_P$  and  $C_S$  are added to the system to ensure that both sides are tuning at the same frequency.  $M$  is the mutual inductance.

When both the primary and secondary sides are tuning at the same frequency, the transferring efficiency  $\eta$  and the power  $P_L$  delivered to the load are expressed as follows [17]:

$$\eta = \frac{R_{\text{ref}}}{R_{\text{ref}} + R_{\text{coil}_P}} \frac{R_L}{R_L + R_{\text{coil}_S}} \quad (1)$$

$$P_L = \eta U_{\text{source}} I_P = I_P^2 \frac{R_{\text{ref}} R_L}{R_L + R_{\text{coil}_S}} \quad (2)$$

where  $R_{\text{ref}}$  is the reflected resistance, which is given by

$$R_{\text{ref}} = \frac{(\omega M)^2}{R_{\text{coil}_S} + R_L} \quad (3)$$

According to (1)-(3), transferring power and efficiency are determined by  $M$ ,  $R_{\text{coil}_P}$ ,  $R_{\text{coil}_S}$ , and  $R_L$  and the resonance angular frequency  $\omega$ . As the EL of seawater is not contained in (1)-(3), applying these equations immediately to analyze the WPT system in seawater is inaccurate. Therefore, analyzing the electric field excited by the current in Coil<sub>Tx</sub> and Coil<sub>Rx</sub> is necessary.

## III. ELECTRIC FIELD IN SEAWATER

The expression of the electric field excited by circular current in coils is deduced in this section. This expression is also verified through experiments via current frequency  $f$ , the root-mean-square (RMS) value of current  $I$ , and coil turns  $N$ . To save time calculating EFI, the expression is simplified to the product of  $f$ ,  $I$ , and  $N$  under the same coil radius. The simplified expression plays an important role in the introduction of EELI in Section IV.

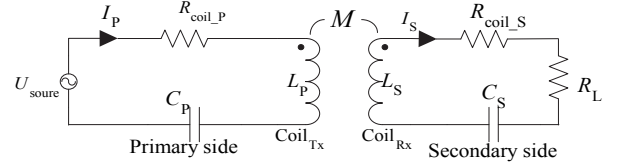


Fig. 1. Circuit model of WPT in air.

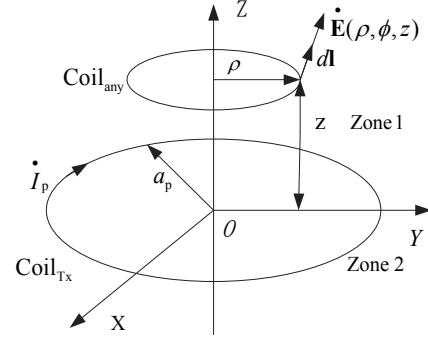


Fig. 2. Electric field excited by circular current.

### A. Inducing the Electric Field Excited by Circular Current

Fig. 2 schematizes a circular current  $\dot{I}_p$  in a coordinate plane XOY with a radius of  $a_p$ . The space is divided into two parts, Zone1 ( $z > 0$ ) and Zone2 ( $z < 0$ ). According to [18], [19], the EFI  $\dot{\mathbf{E}}(\rho, \Phi, z)$  at an arbitrary point  $(\rho, \Phi, z)$  is the solution to the Helmholtz equation in cylindrical coordinates, which is given as follows:

$$\dot{\mathbf{E}}(\rho, \Phi, z) = -j\omega\mu a_p \dot{I}_p N_p \int_0^\infty \frac{\lambda}{u} J_1(\lambda a_p) J_1(\lambda \rho) e^{-u|z|} d\lambda \mathbf{e}_\Phi \quad (4)$$

$J_1$  and  $Y_1$  are the first and secondary species first-order Bessel function.  $u$  is a function of variable  $\lambda$ , permittivity  $\epsilon$ , conductivity  $\sigma$ , and permeability  $\mu$ , which is expressed as

$$u = \sqrt{\lambda^2 - \omega\mu(\omega\epsilon - j\sigma)} \quad (5)$$

$N_p$  is the number of turns of Coil<sub>Tx</sub>. The relationship between  $\dot{I}_p$  and  $I_p$  and between  $\dot{\mathbf{E}}(\rho, \Phi, z)$  and  $E(\rho, \Phi, z)$  are as follows:

$$\begin{cases} \dot{\mathbf{E}}(\rho, \Phi, z) = \sqrt{2} E(\rho, \phi, z) \sin(\omega t + \theta_E) \\ \dot{I}_p = \sqrt{2} I_p \sin(\omega t + \theta_I) \end{cases} \quad (6)$$

where  $E(\rho, \Phi, z)$  is the RMS value of EFI at point  $(\rho, \Phi, z)$ , and  $I_p$  is the RMS value of the current. According to (4), the direction of  $\dot{\mathbf{E}}(\rho, \Phi, z)$  is tangent to Coil<sub>any</sub>. Besides,  $\dot{\mathbf{E}}(\rho, \Phi, z)$  at point  $(\rho, \Phi, z)$  has nothing to do with  $\Phi$ , which indicates that the EFI at any point of Coil<sub>any</sub> in Fig. 2 is the same. Accordingly, the inductive voltage in Coil<sub>any</sub> is as follows:

$$\dot{U}_{\text{inductive}} = \int_{\text{Coil}_{\text{any}}} \dot{\mathbf{E}}(\rho, \phi, z) dl = 2\pi\rho \dot{\mathbf{E}}(\rho, \phi, z) \quad (7)$$

### B. Experiment Verification

To verify whether (4) can be used to calculate EFI, the following experiments are conducted as it is not convenient to measure EFI directly. According to (7), the inductive voltage  $\dot{U}_{\text{inductive}}$  in  $\text{Coil}_{\text{any}}$  is proportional to the EFI. Therefore, we measure  $\dot{U}_{\text{inductive}}$  rather than measure EFI directly.

$\text{Coil}_{\text{any}}$  is kept open. When  $\text{Coil}_{\text{Tx}}$  is excited by  $I_p$ ,  $\dot{U}_{\text{inductive}}$  in  $\text{Coil}_{\text{any}}$  is measured with an oscilloscope. The calculation results of the EFI at any point of  $\text{Coil}_{\text{any}}$  can be calculated through (4).  $\dot{U}_{\text{inductive}}$  is obtained through (7), which requires the EFI at any point of  $\text{Coil}_{\text{any}}$  to be equivalent. Therefore, the coils should be aligned. The numerical calculation results of  $\dot{U}_{\text{inductive}}$  are compared with the experiment results. In the experiments, coils are set as that shown in Fig. 2. Fig. 3 shows the device used to simulate the seawater conditions. The device is composed of two containers filled with saltwater (conductivity  $\sigma \approx 3.3 \text{ S/m}$ ), with radii of 200 and 100 mm, respectively. The height of both containers is 300 mm. As the copper enameled wire is not completely waterproof, coils wound around the smaller container are set in the air gap to insulate the seawater for safety. The container is made of plexiglass and does not influence the electric field excited by  $\text{Coil}_{\text{Tx}}$ . The radii of  $\text{Coil}_{\text{Tx}}$  and  $\text{Coil}_{\text{any}}$  are both 100 mm. According to (4), the EFI in  $\text{Coil}_{\text{any}}$  is determined by the distance to  $\text{Coil}_{\text{Tx}}$ , current RMS value  $I_p$ , coil turns  $N_p$ , and current frequency  $f$ . Afterward, the calculation and experiment results of  $\dot{U}_{\text{inductive}}$  are compared in these four aspects (Fig. 4, Fig. 5, and Fig. 6). Note that, in this paper, “cal” and “exp” represent the calculated and experimental results in the figures, respectively.

Fig. 4 shows the RMS value of  $\dot{U}_{\text{inductive}}$  versus different coil distance  $z$  when the distance  $z$  from  $\text{Coil}_{\text{any}}$  to  $\text{Coil}_{\text{Tx}}$  is varied. The current frequencies are 490, 330, 220, and 110 kHz. All the calculated data in Fig. 4 are obtained under the condition that the number of turns of  $\text{Coil}_{\text{Tx}}$  and  $\text{Coil}_{\text{any}}$  are 14 and 1, respectively, and  $I_p$  is 1.5 A. The RMS value of inductive voltage drops significantly as the distance  $z$  increases, which means that EL is mainly caused by seawater near the coil.

The RMS value of  $\dot{U}_{\text{inductive}}$  versus different  $I_p$  is shown in Fig. 5. The current frequencies are also 490, 330, 220, and 110 kHz, respectively. All the calculated data in Fig. 5 are obtained under the condition that the number of turns of  $\text{Coil}_{\text{Tx}}$  and  $\text{Coil}_{\text{any}}$  are 14 and 1, respectively, and the distance between  $\text{Coil}_{\text{Tx}}$  and  $\text{Coil}_{\text{any}}$  is 35 mm.

The RMS value of  $\dot{U}_{\text{inductive}}$  versus different current frequency  $f$  is shown in Fig. 6. The turns of  $\text{Coil}_{\text{Tx}}$  are 17, 14, and 11, respectively. All the calculated data in Fig. 6 are obtained under the condition that the number of turns of  $\text{Coil}_{\text{any}}$  is 1, the distance between  $\text{Coil}_{\text{Tx}}$  and  $\text{Coil}_{\text{any}}$  is 35 mm, and the current  $I_p$  is 1.5A.

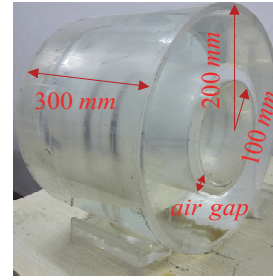


Fig. 3. Device used to simulate seawater conditions.

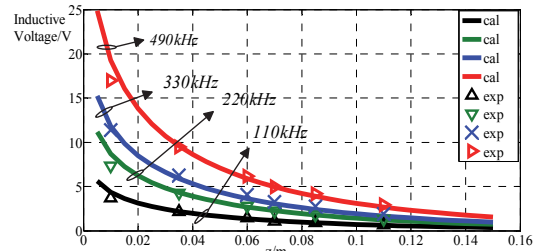


Fig. 4. Inductive voltage versus  $z$  at different frequencies in seawater.

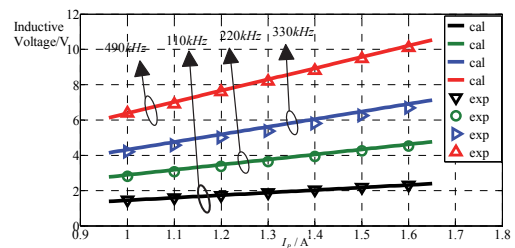


Fig. 5. Inductive voltage versus  $I_p$  at different frequencies in seawater.

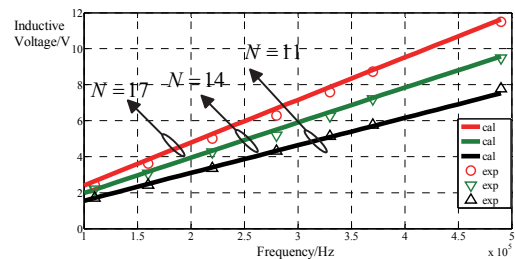


Fig. 6. Inductive voltage versus frequency at different turns of  $\text{Coil}_{\text{Tx}}$  in seawater.

Fig. 4, Fig. 5, and Fig. 6 show that the calculation results are in accordance with the experiment results. The errors between calculation and experiment results are under 8%, which indicates that (4) can be used to calculate the EFI in seawater. Equation (4) reveals that the EFI is proportional to  $I_p$  and  $N_p$ . Although determining the relationship between frequency  $f$  and the EFI through (4) is difficult, Fig. 6 illustrates that EFI is proportional to  $f$ . This finding indicates that  $f$  does not significantly influence the result of the integral part in (4). Thus, (4) is simplified to the following equation:

$$E(\rho, \phi, z) \approx k_E(\rho, \phi, z) N_p f I_P \quad (8)$$

where  $k_E$  is the coefficient at point  $(\rho, \Phi, z)$ , which is related to the coil radius and coil shape. As the eddy current loss (ECL) is the volume integral of  $E$ , it is time-consuming to analyze ECL through (4). In designing the WPT system, we are mainly concerned with the influence of  $f$ ,  $I_p$ , and  $N_p$  on ECL. The EFI presented through (8) will simplify the derivation of the equivalent ECL impedance in the next section.

#### IV. EDDY LOSS ANALYSIS IN SEAWATER

In Section III, the EFI excited by single coil  $\text{Coil}_{\text{Tx}}$  is analyzed. In this section, the synthesized EFIs excited by both primary and secondary coils are analyzed. The EELI, which is the foundation for setting up the model of the WPT system in seawater, is also introduced into the WPT system.

##### A. Synthesized EFI Excited by Primary and Secondary Current

Similar to  $\text{Coil}_{\text{Tx}}$  in Fig. 2, both the current in primary coil  $\dot{I}_P$  and in secondary coil  $\dot{I}_S$  excite the electric field. Fig. 7 is the schematic diagram of the EFI.  $\dot{E}_P$  is excited by  $\dot{I}_P$  and  $\dot{E}_S$  is excited by  $\dot{I}_S$ .  $\text{Coil}_{\text{Tx}}$  and  $\text{Coil}_{\text{Rx}}$  represent the primary and secondary coils, respectively. The coil radii are  $a_p$  and  $a_s$ . The coordinates of each coil central are  $(0, 0, -h)$  and  $(0, 0, h)$ .

According to (4),  $\dot{E}_P$  and  $\dot{E}_S$  at any point  $(\rho, \Phi, z)$  can be expressed as

$$\begin{cases} \dot{E}_P(\rho, \Phi, z) = \sqrt{2} E_P \sin(\omega t + \theta_1) \mathbf{e}_\Phi \\ = -j\omega\mu a_p N_p I_P \int_0^\infty \frac{\lambda}{u} J_1(\lambda a_p) J_1(\lambda \rho) e^{-u|z+h|} d\lambda \mathbf{e}_\Phi \\ \dot{E}_S(\rho, \Phi, z) = \sqrt{2} E_S \sin(\omega t + \theta_2) \mathbf{e}_\Phi \\ = -j\omega\mu a_s N_s I_S \int_0^\infty \frac{\lambda}{u} J_1(\lambda a_s) J_1(\lambda \rho) e^{-u|z-h|} d\lambda \mathbf{e}_\Phi \end{cases} \quad (9)$$

where  $N_p$  and  $N_s$  are the coil turns of the primary and secondary coils. The synthesized electric field  $\dot{E}_{\text{total}}$  at point  $(\rho, \Phi, z)$  is the vector sum of  $\dot{E}_P(\rho, \Phi, z)$  and  $\dot{E}_S(\rho, \Phi, z)$ :

$$\begin{aligned} \dot{E}_{\text{total}}(\rho, \Phi, z) &= \dot{E}_P(\rho, \Phi, z) + \dot{E}_S(\rho, \Phi, z) \\ &= \sqrt{2} E_{\text{total}} \sin(\omega t + \theta_3) \mathbf{e}_\Phi \end{aligned} \quad (10)$$

Therefore, the EL is as follows [12], [20]:

$$P_{\text{eddy}} = \iiint_V \sigma_{\text{sea}} E_{\text{total}}^2 dV \quad (11)$$

where  $V$  is the EL zone. Although EL can be calculated through (9)-(11), such operation is too computationally intensive. Moreover, both the primary and secondary sides are related to EL according to (9)-(11).

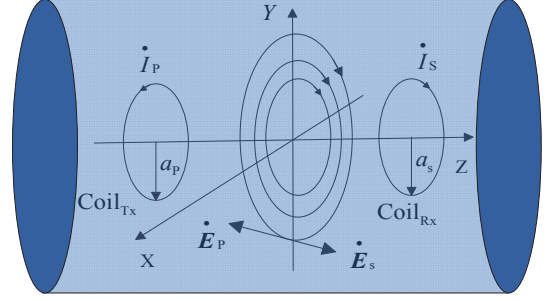


Fig. 7. Electric field excited by  $\dot{I}_P$  and  $\dot{I}_S$ .

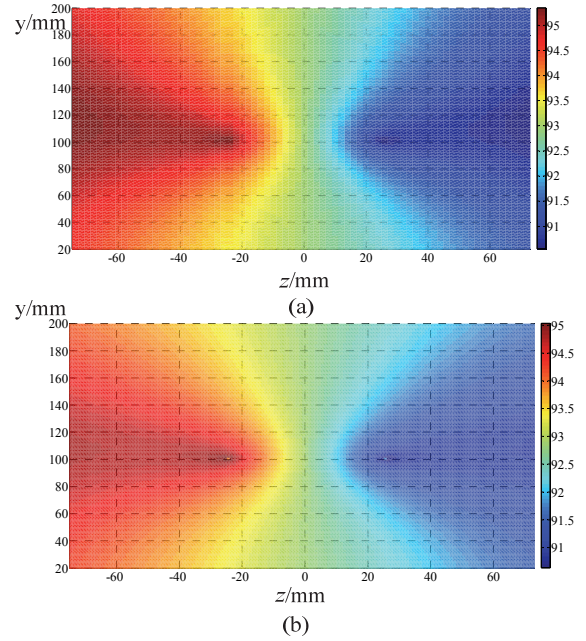


Fig. 8. Phase difference of  $\dot{E}_P(\rho, \Phi, z)$  and  $\dot{E}_S(\rho, \Phi, z)$ : (a) Calculated results and. (b) Finite element analysis results.

##### B. Simulation and Experiment Verification

The phase difference  $\theta_{PS}$  of  $\dot{E}_P(\rho, \Phi, z)$  and  $\dot{E}_S(\rho, \Phi, z)$  is shown in Fig. 8. Fig. 8(a) is the calculated results using (9), while Fig. 8(b) is the result of the finite element analysis using COMSOL. The parameters for simulation and calculation are as follows:  $\text{Coil}_{\text{Tx}}$  and  $\text{Coil}_{\text{Rx}}$  are set as shown in Fig. 7, frequency is 300 kHz, coil gap is 50 mm, and coil radii are 100 mm. A comparison of Figs. 8(a) and (b) shows that the calculated results are close to the finite element analysis results. The phase difference between  $\dot{E}_P(\rho, \Phi, z)$  and  $\dot{E}_S(\rho, \Phi, z)$  is also close to  $90^\circ$ . With  $\theta_{PS}$  close to  $90^\circ$ ,  $E_{\text{total}}$  in (10) and (11) is expressed as follows:

$$E_{\text{total}} \approx \sqrt{E_S^2 + E_P^2} \quad (12)$$

##### C. Equivalent Eddy Loss Impedance

###### 1) Basic Equivalent

For the purpose of setting up the power distribution model of the WPT system in seawater, EELI is introduced to solve

these problems. When (12) is substituted into (11), the total eddy loss is obtained as follows:

$$P_{\text{eddy}} = \iiint_V \sigma_{\text{sea}} (E_p^2 + E_s^2) dV \quad (13)$$

From (13), the EL of the WPT system is composed of two parts, one caused by primary side  $\vec{E}_p$  and the other by  $\vec{E}_s$ . According to (8), the ELs caused by primary side ( $P_{\text{eddy}_p}$ ) and secondary side ( $P_{\text{eddy}_s}$ ) can be expressed as

$$\begin{cases} P_{\text{eddy}_p} = \iiint_V \sigma(k_E(\rho, \phi, z) N_p f I_p)^2 dV \\ \quad = R_{\text{eddy}_p} I_p^2 \\ P_{\text{eddy}_s} = \iiint_V \sigma(k_E(\rho, \phi, z) N_s f I_s)^2 dV \\ \quad = R_{\text{eddy}_s} I_s^2 \end{cases} \quad (14)$$

where

$$\begin{cases} R_{\text{eddy}_p} = N_p^2 f^2 \iiint_V \sigma k_E(\rho, \phi, z)^2 dV \\ \quad = k_{\text{eddy}_p} N_p^2 f^2 \\ R_{\text{eddy}_s} = N_s^2 f^2 \iiint_V \sigma k_E(\rho, \phi, z)^2 dV \\ \quad = k_{\text{eddy}_s} N_s^2 f^2 \end{cases} \quad (15)$$

$k_E$  at any point  $(\rho, \Phi, z)$  can be calculated by using (4). According to (4),  $k_E$  is determined by  $a_p$ ,  $\rho$ , and  $z$  and does not change with the current. Thus,  $k_{\text{eddy}_p}$  and  $k_{\text{eddy}_s}$  are constant as long as  $\sigma$ ,  $\mu$ ,  $\epsilon$ ,  $a_p$ ,  $a_s$ , and so forth do not change.  $R_{\text{eddy}_p}$  and  $R_{\text{eddy}_s}$  in (15) are defined as the EELI.

For the purpose of improving the transfer efficiency as high as possible, ECL needs to be calculated many times to find the optimum values of  $f$ ,  $N_p$ , and  $N_s$ . In searching for the optimum  $f$ ,  $N_p$  and  $N_s$ , it is really time-consuming to calculate ECL via (14). Given that  $k_{\text{eddy}_p}$  and  $k_{\text{eddy}_s}$  are unknown, the ECL should be calculated through (4) and (14) for the first time. Once ECL is obtained,  $k_{\text{eddy}_p}$  and  $k_{\text{eddy}_s}$  can be calculated through (14). As long as  $k_{\text{eddy}_p}$  and  $k_{\text{eddy}_s}$  are known, the EELI at different  $f$ ,  $N_p$ , or  $N_s$  can be determined through (15). The ECL can likewise be calculated through (14).

## 2) Influence of Coil Radius to EELI

In some cases, the coil radius may also change. However, (15) can only be applied to calculate the EELI at different numbers of turns and frequencies. To extend (15) into calculating the EELI at different radii, the distribution characters of EFIs excited by coils with different radii are compared. TABLE I presents parameters of the two coils. The RMS value of EFI from point  $(r, \pi/2, -0.66r)$  to  $(r, \pi/2, 0.66r)$  is depicted in Fig. 10(a) and that from point  $(0, \pi/2, 0)$  in Fig. 10(b). Although the radii are different,

TABLE I  
PARAMETERS OF THE TWO COILS

	$N$	$I/A$	$f/\text{kHz}$	$r/\text{mm}$
Coil <sub>1</sub>	14	1	750	180
Coil <sub>2</sub>	7	2	750	60

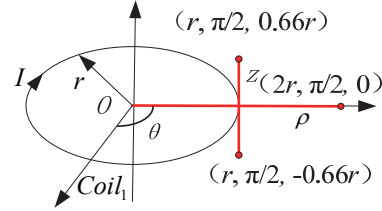
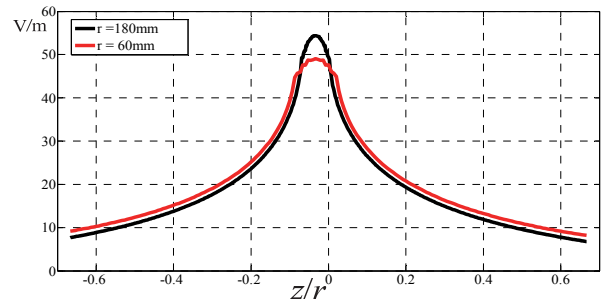
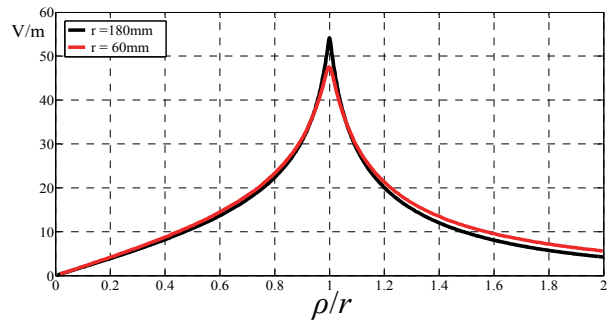


Fig. 9. Normalized cylindrical coordinate system.



(a)



(b)

Fig. 10. Comparison of EFI excited by coils with different radii.

the distribution characters of EFI in Coil<sub>1</sub> and Coil<sub>2</sub> are the same (Fig. 10). The normalized distribution of EFIs is also the same when  $N_1 I_1 f_1$  is equivalent to  $N_2 I_2 f_2$ . Hence, the integrate volume  $V$  increases with coil radius  $r$  in a certain index  $x$ , and the relationship between each coefficient is as follows:

$$k_{\text{eddy}_r1} = k_{\text{eddy}_r2} (\eta_1 / r_2)^x \quad (16)$$

where  $k_{\text{eddy}_r1}$  and  $k_{\text{eddy}_r2}$  are the coefficients of EELI to coils with radii  $r_1$  and  $r_2$ , respectively.

According to (15), the EELI of coils with radius  $r_1$  and coil turns  $N_1$  at frequency  $f_1$  can be expressed as follows:

$$R_{\text{eddy}_r1}(f_1, N_1) = (\eta_1 / r_2)^x (N_1 / N_2)^2 \cdot (f_1 / f_2)^2 R_{\text{eddy}_r2}(f_2, N_2) \quad (17)$$

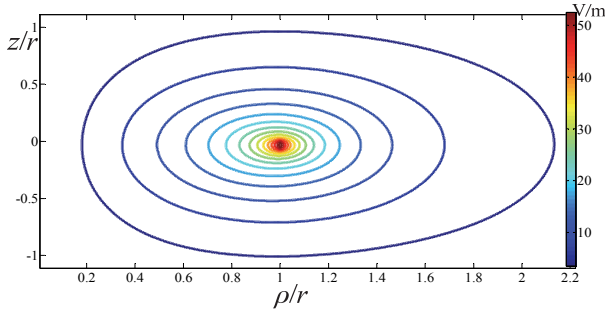
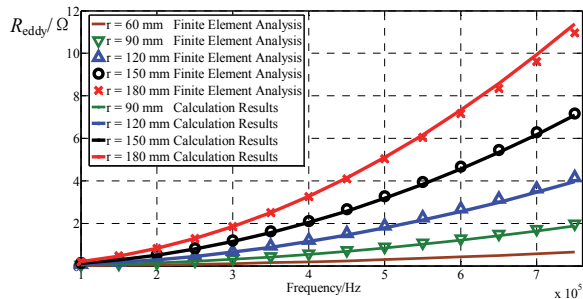
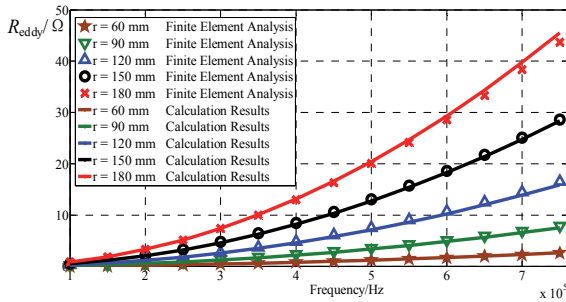


Fig. 11. Equipotential of EFI.



(a)  $N_1 = 7$ .



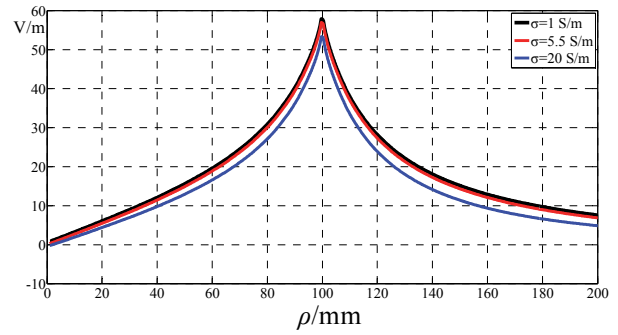
(b)  $N_1 = 14$ .

Fig. 12. EELI with different coil radii.

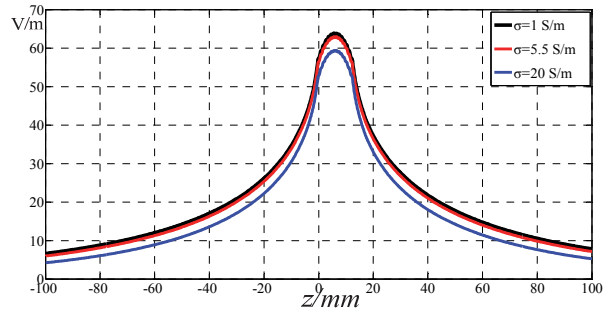
where  $R_{eddy\_r2}(f_2, N_2)$  is the EELI of the coil with radius  $r_2$  and coil turns  $N_2$  at frequency  $f_2$ . Once  $R_{eddy\_r2}(f_2, N_2)$  is obtained, the EELI at different radii can be calculated. The equipotential of EFI excited by Coil<sub>1</sub> is shown in Fig. 11. The shape of the outer equipotential is ellipse-like. Finding the relationship between the index  $x$  in (17) and the coil radius is difficult, but we find that  $x$  can be set as 2.6. The EELIs with different coil radii are shown in Fig. 12. The calculated results are obtained through (17), and the parameters  $r_2$  and  $N_2$  are 60 mm and 7 turns. In Fig. 12 (a), the coil turn  $N_1$  is 7, and in Fig. 12(b),  $N_1$  is 14. The calculated results are close to the finite element analysis results in Fig. 12, indicating that (17) can be used to calculate EELI at different radii.

### 3) Influence of Conductivity on EELI

According to (13), the power lost in seawater is proportional to conductivity  $\sigma$ . However, this condition is not always true because the influence of  $\sigma$  on EFI should also be considered, especially when the frequency or the conductivity is high. The EFI at different conductivities is shown in Fig. 13. The parameters of finite element analysis are as follows:

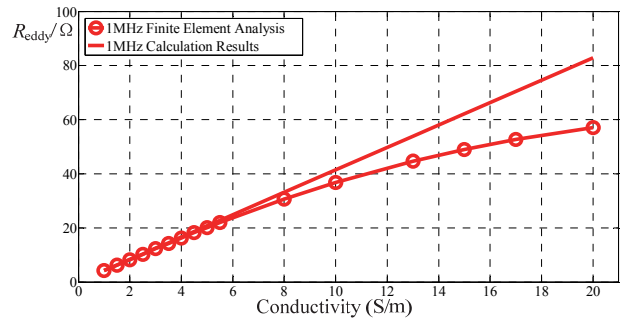


(a)

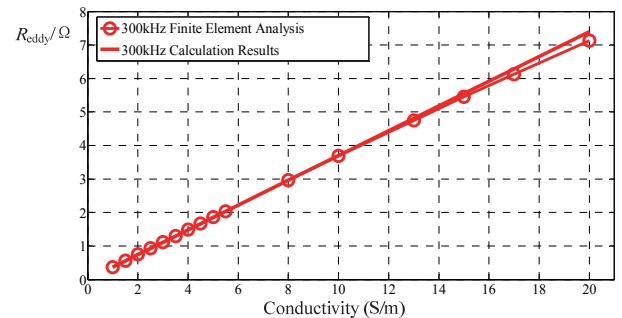


(b)

Fig. 13. EFI at different conductivities  $\sigma = 1$  S/m,  $\sigma = 5.5$  S/m,  $\sigma = 20$  S/m: (a) Comparison in direction  $\rho$ . (b) Comparison in direction  $z$ .



(a)



(b)

Fig. 14. EELI at different conductivities: (a) 1 MHz frequency. (b) 330 kHz frequency.

frequency is 1 MHz, current is 1 A, and number of turns is 14. A comparison of the EFIs in direction  $\rho$  [Fig. 13(a)] and direction  $z$  [Fig. 13(b)] shows that the EFI diminishes while the conductivity increases from 5.5 S/m to 20 S/m. However,

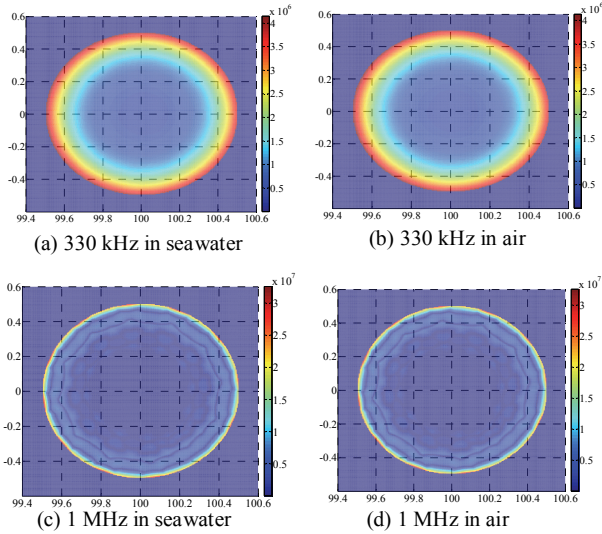


Fig. 15. Current density in wire.

it can be seen from Fig. 13 that the EFIs are almost the same between  $\sigma=1$  S/m and  $\sigma=5.5$  S/m.

As shown in Fig. 14(a), the EELI is almost proportional to  $\sigma$  while the conductivity is less than 8 S/m. However, the influence of conductivity on diminishing EFI cannot be ignored because  $\sigma$  is larger than 10 S/m. When the frequency is 300 kHz, the EELI is almost proportional to conductivity (less than 20 S/m), as shown in Fig. 14(b). Therefore, the application of (15) is constrained by the frequency or the medium conductivity. In addition, the conductivity of seawater is approximately 4 S/m, and if the resonance frequency of the WPT system is under 1 MHz, the EELI can be calculated using (15) in seawater.

#### 4) Experiment Verification

Fig. 15 shows the current density in wire, while the frequencies are 330 kHz and 1 MHz in air and seawater. The number of turns is 1, and the current in wire is 1 A. When the current frequency is the same, the loss in coil should be equal in air and seawater because the current densities are almost the same. Therefore, it is reasonable to consider that the coil resistance  $R_{\text{coil}}$  is constant in both air and seawater at the same frequency.

Fig. 16 shows the simulated, calculated, and measured EELI when the numbers of turns are 11, 14, and 17, respectively, and the coil radii are all 100 mm. The simulated results are obtained by using finite element analysis. Two steps can be used to measure ELI. First, the coil is put in air and its coil resistance  $R_{\text{coil\_air}}$  is measured using the Impedance Analyzer WK6500B. Second, the coil is put in the container shown in Fig. 3 and the total resistance of the coil  $R_{\text{total\_sea}}$  is measured. The measured EELI is obtained by the following equation:

$$R_{\text{eddy}} = R_{\text{total\_sea}} - R_{\text{coil\_air}}$$

To calculate the EELI, the factor  $k_{\text{eddy}}$  should be calculated first using (9) and (14). Next, the EELI at different frequencies

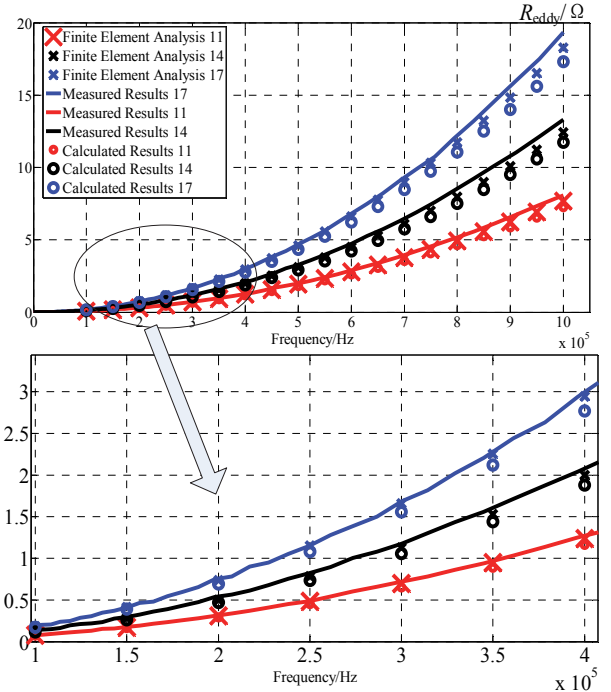


Fig. 16. Simulated, calculated, and measured results of EELI.

and coil turns can be established by utilizing (15). The  $k_{\text{eddy}}$  used to calculate the EELI in Fig. 16 is  $5.988 \times 10^{-14}$ , which is obtained at the frequency of 330 kHz. The calculated results are close to the measured results, indicating that (15) can be applied to calculate the EELI.

Improving transfer efficiency is one of the most important issues in designing the WPT system. Identifying the highest efficiency parameters, such as number of turns and frequency, through experiments is time consuming. As the EELI can be calculated, the optimizing process can be realized by using MATLAB rather than experiments.

## V. POWER DISTRIBUTION MODEL OF THE WPT SYSTEM

In this section, the power distribution model in seawater is given. Owing to the influence of seawater, the consumed power in the WPT system is classified into five parts and is verified through experiments.

### A. Basic Circuit Model

When EELI is taken into consideration, the basic circuit model of WPT system in seawater is different from what is shown in Fig. 1. The circuit model for the underwater system is depicted in Fig. 17, where all the parameters have the same meaning as in Fig. 1, except for the newly added  $R_{\text{eddy\_p}}$  and  $R_{\text{eddy\_s}}$ , which can be obtained through (15).

The EELI expression was induced in Section IV. To analyze the total power loss, it is necessary to know the coil resistance. Coil resistance is composed of DC resistance and

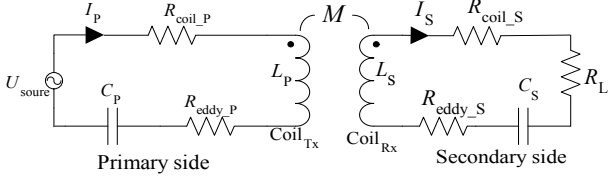


Fig. 17. Circuit model of the WPT system in seawater.

AC resistance. AC resistance increases with frequency as a consequence of skin effects and proximity effects. Numerous methods can be used to calculate the resistance of circular spiral coil [21], [22], but deducing a precise equation to calculate the resistance of the helical coil used in our experiments is difficult. In the present study, coil resistance is obtained through curve fitting. Coil resistance is initially calculated through finite element analysis. By comparing the resistances of coils with different numbers of turns and frequencies, we find that coil resistance can be calculated by the following function:

$$R_{\text{coil}}(f, N) = R_{\text{coil}}(f, 2) \times (N - 2) \times \left(\frac{f}{f_0}\right)^{0.235} (N \geq 3) \quad (18)$$

where  $f$  is the frequency and  $N$  is the number of turns. As the frequencies used in the experiments are all above 100 kHz, this value is chosen as the  $f_0$ .  $R_{\text{coil}}(f, 2)$  is the finite element analysis results of coil resistance at frequency  $f$ , while the coil turn is 2. Once  $R_{\text{coil}}(f, 2)$  is obtained through finite element analysis, (18) can be applied to calculate coil resistance at different turns and frequencies. The simulated results of  $R_{\text{coil}}(f, 2)$  are shown in Fig. 18. The measured, calculated, and finite element analysis results of coil resistance when the coil turns are 11, 14, and 17, respectively, are shown in Fig. 18. The measured results are obtained through an impedance analyzer. The calculated and measured results are close. Therefore, (18) can be used in the optimization procedure in Section VI.

According to Fig. 17, the input power is absorbed by five parts:

$$\begin{aligned} P_{\text{in}} &= P_{\text{coil}_P} + P_{\text{eddy}_P} + P_{\text{coil}_S} + P_{\text{eddy}_S} + P_L \\ &= I_P^2 R_{\text{coil}_P} + I_P^2 R_{\text{eddy}_P} + I_S^2 R_{\text{coil}_S} + I_S^2 R_{\text{eddy}_S} + I_S^2 R_L \end{aligned} \quad (19)$$

Deriving from equations (15) and (19), the power delivered to the load and transfer efficiency in seawater are given as follows:

$$P_L = I_S^2 R_L = I_P^2 \frac{R_{\text{ref}} R_L}{R_L + R_{\text{coil}_S} + R_{\text{eddy}_S}} \quad (20)$$

$$\eta = \frac{I_S^2 R_L}{P_{\text{in}}} = \frac{R_{\text{ref}}}{R_{\text{ref}} + R_{\text{coil}_P} + R_{\text{eddy}_P}} \frac{R_L}{R_L + R_{\text{coil}_S} + R_{\text{eddy}_S}} \quad (21)$$

Equations (19)-(21) are the power distribution model in seawater. The power distribution model is the foundation for parameter optimization to improve transfer efficiency in Section VI.

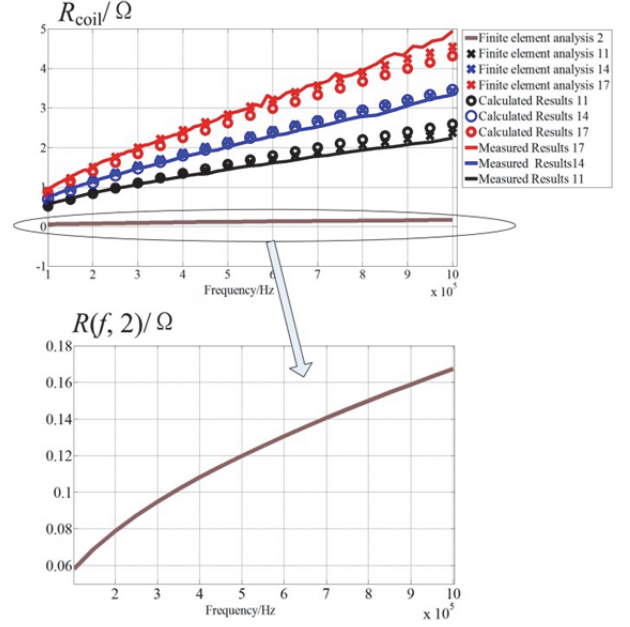


Fig. 18. Coil resistance of different turns versus frequency.

### B. Experiment Verification

To verify the power distribution model, a WPT experiment is conducted with  $N_p = N_s = 14$  and  $R_L = 20.5 \Omega$ . The coil gap between primary and secondary sides is 50 mm. The mutual inductance between primary and secondary coils is 20.0  $\mu\text{H}$ . Given that the number of turns and radii in the primary and secondary sides are the same,  $R_{\text{eddy}_P}$  is considered to be equal to  $R_{\text{eddy}_S}$ . Thus,  $R_{\text{coil}_P}$  is equal to  $R_{\text{coil}_S}$ .  $R_{\text{eddy}_P}$ ,  $R_{\text{eddy}_S}$  and  $R_{\text{coil}_P}$ ,  $R_{\text{coil}_S}$  are obtained from (15) and (18), respectively.  $U_{\text{source\_air}}$  is the power source voltage, while the WPT experiment is conducted in air.  $U_{\text{source\_sea}}$  is measured while the experiment is conducted in a container, as shown in Fig. 3.  $I_S$  is constant at 1.5 A, but  $I_P$  has to be changed to ensure  $I_S$  is 1.5 at different frequencies. The current  $I_P$  and  $I_S$  are measured through the current probe Tektronix TCP0020.

The total power provided by the power source is shown in Fig. 19. The calculated input power is obtained through (19). The measured power provided by the power source is calculated as follows:

$$P_{\text{Measured\_air}} = U_{\text{source\_air}} I_{P\_air}$$

$$P_{\text{Measured\_sea}} = U_{\text{source\_sea}} I_{P\_sea}$$

where  $I_{P\_air}$  and  $I_{P\_sea}$  are the measured results of  $I_P$  in air and seawater, respectively. As the power delivered to the load is the same, the total input power of the WPT system in seawater is larger than that in air because a part of the energy is lost in seawater. The calculated results are close to the measured results, which suggest that the power distribution model proposed in this paper can be applied to the analysis of the WPT system in seawater.

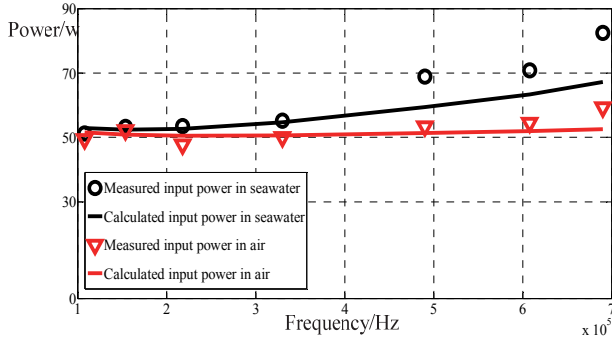


Fig. 19. Power in air and seawater at different frequencies.

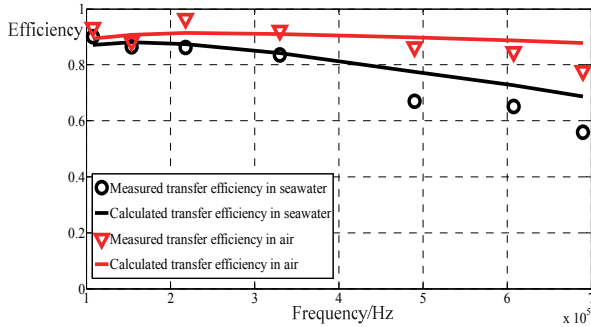


Fig. 20. Efficiencies in air and seawater at different frequencies.

The measured efficiencies in Fig. 20 are calculated as follows:

$$\eta_{\text{Measured\_air}} = R_L I_S^2 / U_{\text{source\_air}} P_{\text{air}}$$

$$\eta_{\text{Measured\_sea}} = R_L I_S^2 / U_{\text{source\_sea}} P_{\text{sea}}$$

The calculated efficiencies are obtained from (21). A comparison of the transfer efficiencies in air and seawater in 0 reveals that the EL has a slight influence on efficiency when the frequency is under 300 kHz because the EELI is small. The difference of efficiencies in air and seawater increases with frequency. When the frequency is over 400 kHz, the transfer efficiency in air is almost 10% higher than that in seawater, indicating that the ECL remarkably influences the transfer efficiency. Compared with the red line, the black line in Fig. 20 is the calculation results with the EELI considered. Therefore, to optimize the parameters of the WPT system seawater, the eddy loss should be considered and the power distribution model used as the foundation.

Note that the error between measured and calculated results increases as the frequency increases, which is caused by the loss in the connection wire, capacitance, and so on. To simplify the power distribution model, the power lost in the conducted wire is ignored because it is minimal when the frequency is under 450 kHz. To ensure high transferring efficiency in seawater, the resonant frequency is usually under 300 kHz. Therefore, it is reasonable to ignore the conducted wire loss.

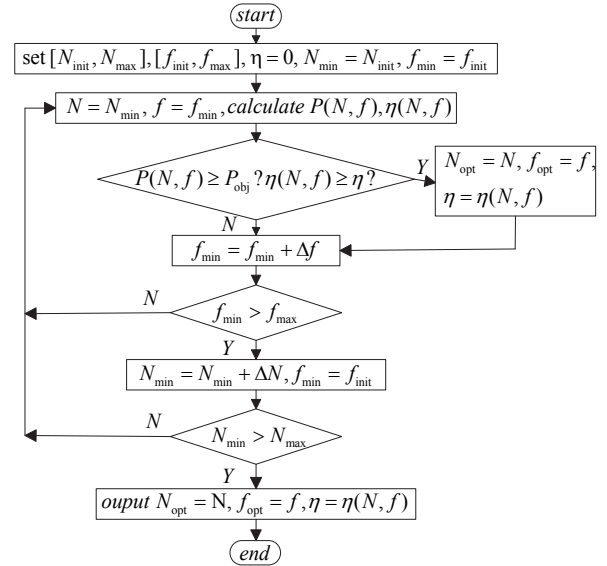


Fig. 21. Flow chart of parameter optimization.

## VI. OPTIMIZATION OF THE WPT SYSTEM IN SEAWATER

The coil radius is usually constant under the volume restriction of underwater vehicles. Apparently, the distance should be as small as possible for high transfer efficiency. For this reason, the transfer distance is settled in the application. The optimization parameters are resonance frequency  $f$  and coil turns  $N$ . The goal of optimization is to maximize efficiency ensuring that the power delivered to the load is satisfactory, which can be described as follows:

$$\begin{cases} P_{\text{opt}}(f_{\text{opt}}, N_{\text{opt}}) \geq P_{\text{obj}} \\ \eta_{\text{opt}}(f_{\text{opt}}, N_{\text{opt}}) = \max\{\eta(f, N)\} \\ U_{\text{opt}} \leq U_{\text{max}} \end{cases} \quad (22)$$

where  $P_{\text{obj}}$  is the required power delivered to load,  $U_{\text{max}}$  is the maximum output voltage of power source, and  $P_{\text{opt}}$  and  $\eta_{\text{opt}}$  are the optimization results of load power and efficiency. The searching process is shown in Fig. 21.  $P(f, N)$  and  $\eta(f, N)$  in Fig. 21 are calculated according to the power distribution model in Section V. TABLE II gives the parameters of the optimized WPT system under the condition of  $R_L = 20.5 \Omega$ ,  $a_p = a_s = 100 \text{ mm}$ , coil gaps 30 mm, and  $P_{\text{obj}} = 100 \text{ W}$ ,  $U_{\text{max}} = 55 \text{ V}$ . We intend to supply power to the battery through the WPT system. The equivalent load in the input side of the rectifier is about 20 ohms, while the power delivered to the battery is 100 W. This is the reason 20.5 ohms is chosen as the object load for optimization.

Fig. 22 shows a picture of the experiment. The waveforms of  $\dot{U}_{\text{source}}$ ,  $\dot{I}_p$ , and  $\dot{I}_s$  are presented in Fig. 23. The calculated and experimental efficiencies versus frequency are shown in Fig. 24. The transfer efficiencies vary with different groups of  $(N, f)$ . Taking Fig. 24 for example, the transfer efficiency drops from the highest point of 95% at 107 kHz to 85% at

TABLE II  
PARAMETERS OF THE OPTIMIZED WPT SYSTEM

Parameters	Value
$L_p/\mu\text{H}$	131.99
$L_s/\mu\text{H}$	131.64
$C_p/\text{nF}$	15
$C_s/\text{nF}$	15
$N_p, N_s$	17
Coil Gap/mm	30
Wire Diameter/mm	0.84
Coil Radius/mm	100
$R_l/\Omega$	20.5
Frequency/kHz	107.1

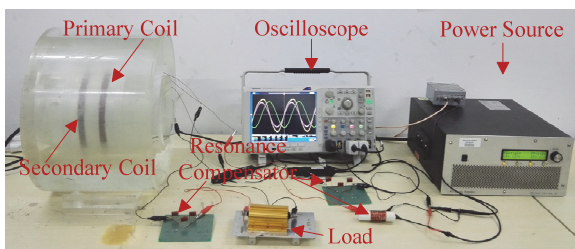


Fig. 22. Picture of the experiment.

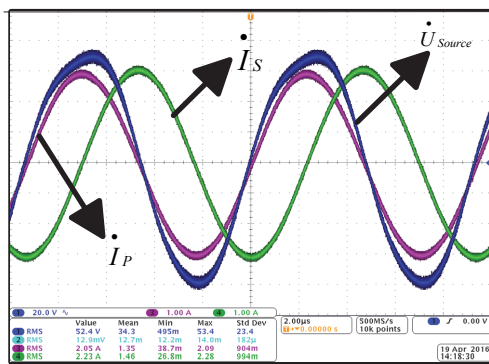


Fig. 23. Waveforms of  $\dot{U}_{source}$ ,  $\dot{I}_p$ , and  $\dot{I}_s$ .

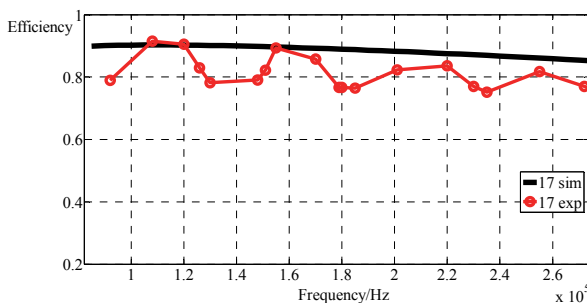


Fig. 24. Calculated and experimental efficiencies versus frequency when  $N_p = N_s = 17$ .

260 kHz. If the transfer efficiency is not known in advance, we will then have to test the efficiencies one by one to find the highest point. This task would be time-consuming. Without

the guidance of an optimization method, designers may also be able to figure out a reasonable group of  $(N, f)$ , though whether this group is the best is unknown. Compared the highest and lowest points in Fig. 24, the difference of efficiencies may be 10%. With the help of an optimization method, designers will be able to obtain the optimum parameters quickly. The calculated efficiency is close to the experiment results, which means that the optimized process can be used in the design of the WPT system in seawater.

## VII. CONCLUSIONS

In this study, the EFI excited by circular current in seawater is analyzed and is used as the foundation to analyze the EL of a WPT system. The EELI is added to the circuit model to calculate the EL in seawater. A brief method to calculate EELI is given, which can be applied when the frequency is under 1 MHz and the conductivity is under 8 S/m. The proposed power distribution model in seawater is composed of five parts (load power, coil, and EL on both sides) and can be applied in the analysis of power delivered to load and the transfer efficiency of WPT systems. The power distribution model is also the foundation for optimizing the WPT system in seawater. The method of parameter optimization for maximizing transferring efficiency is presented under the condition of fixed load, coil gap, coil radii, and power delivered to the load. According to the optimization flow chart, a WPT system is fabricated with greater than 90% power transfer efficiency, a gap of 30 mm, and a frequency of 107.1 kHz.

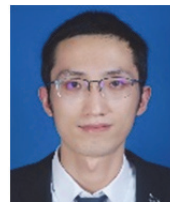
## REFERENCES

- [1] T. McGinnis, C. P. Henze, and K. Conroy, "Inductive power system for autonomous underwater vehicles," in *Proc. IEEE Oceans Conf.*, pp. 1-5, 2007.
- [2] R. Itoh, Y. Sawahara, T. Ishizaki, and I. Awai, "Wireless power transfer to moving ornamental robot fish in aquarium," in *Proc. IEEE 3rd Global Conference on Consumer Electrics (GCCE)*, pp. 459-460, 2014.
- [3] T. Assaf, C. Stefanini, and P. Dario, "Autonomous underwater biorobots: A Wireless system for power transfer," *IEEE Robot. Autom. Mag.*, Vol. 20, No. 3, pp. 26-32, Sep. 2013.
- [4] S. Aldhaher, C. K. Luk, K. E. K. Drissi, and J. F. Whidborne, "High-input-voltage high-frequency class E rectifiers for resonant inductive links," *IEEE Trans. Power Electron.*, Vol. 30, No. 3, pp. 1328-1335, Mar. 2015.
- [5] Y. J. Kim, D. Ha, W. J. Chappell, and P. P. Irazoqui, "Selective wireless power transfer for smart power distribution in a miniature-sized multiple-receiver system," *IEEE Trans. Ind. Electron.*, Vol. 63, No. 3, pp. 1853-1862, Mar 2016.
- [6] T. Kojiya, F. Sato, H. Matsuki, and T. Sato, "Construction of non-contacting power feeding system to underwater vehicle utilizing electromagnetic induction," in *Proc. IEEE Europe Oceans Conf.*, pp. 709-712, 2005.

- [7] C. M. Baer, M. Alten, G. Bixler, L. Fredette, J. Owens, G. Purvinis, J. Schaefer, and G. Stou, "Non-contact wet mateable connector," in *Proc. IEEE Oceans Conf.*, pp. 1-6, 2009.
- [8] H. Fukuda, N. Kobayashi, K. Shizuno, S. Yoshida, M. Tanomura, and Y. Hama, "New concept of an electromagnetic usage for contactless communication and power transmission in the ocean," in *Proc. IEEE Underwater Technology Symposium Conf.*, pp. 1-4, 2013.
- [9] G. V. Tibajia and M. C. R. Talampas, "Development and evaluation of simultaneous wireless transmission of power and data for oceanographic devices," in *Proc. IEEE Sensors Conf.*, pp. 254-257, 2011.
- [10] M. Ogihara, T. Ebihara, K. Mizutani, and N. Wakatsuki, "Wireless power and data transfer system for station-based autonomous underwater vehicles," in *Proc. IEEE Oceans*, pp. 1-5, 2015.
- [11] V. Bana, M. Kerber, G. Anderson, and J. D. Rockway, "Underwater wireless power transfer for maritime applications," in *Proc. IEEE Wireless Power Transfer Conference*, pp. 1-4, 2015.
- [12] Z. Cheng, Y. Lei, K. Song, and C. Zhu, "Design and loss analysis of loosely coupled transformer for an underwater high-power inductive power transfer system," *IEEE Trans. Magn.*, Vol. 51, No. 7, Jul. 2015.
- [13] J. Zhou, D. J. Li, and Y. Chen, "Frequency selection of an inductive contactless power transmission system for ocean observing," *Ocean Engineering*, Vol. 60, No. 3, pp. 175-185, Mar. 2013.
- [14] S. Raju, R. Wu, M. Chan, and C. P. Yue, "Modeling of mutual coupling between planar inductors in wireless power applications," *IEEE Trans. Power Electron.*, Vol. 29, No. 1, pp. 481-490, Jan. 2014.
- [15] H. J. Choi, S. Lee, and C. Cha, "Optimization of geometric parameters for circular loop antenna in magnetic coupled wireless power transfer," in *Wireless Power Transfer Conference*, pp. 280-283, 2014.
- [16] S. Raju, C. C. Prawoto, M. Chan, and C. P. Yue, "Modeling of on-chip wireless power transmission system," in *Proc. IEEE Wireless Symposium*, pp. 1-4, 2015.
- [17] W. X. Zhong, C. Zhang, X. Liu, and S. Y. R. Hui, "A methodology for making a three-coil wireless power transfer system more energy efficient than a two-coil counterpart for extended transfer distance," *IEEE Trans. Power Electron.*, Vol. 30, No. 2, pp. 933-942, Feb. 2015.
- [18] K. Zhang, L. Du, Z. Zhu, B. Song, and D. Xu, "A normalization method of delimiting the electromagnetic hazard region of a wireless power transfer system," *IEEE Trans. Electromagn. Compat.*, to be published.
- [19] M. A. K. Hamid, W. M. Boerner, L. Shafai, S. J. Towajj, W. P. Alsip, and G. J. Wilson, "Radiation characteristics of bent-wire antennas," *IEEE Trans. Electromagn. Compat.*, Vol. EMC-12, pp. 106-111, Aug. 2007.
- [20] K. H. Zhang, L. B. Yan, Z. C. Yan, H. B. Wen, and B. W. Song, "Modeling and analysis of eddy-current loss of underwater contact-less power transmission system based on magnetic coupled resonance," *Acta Physica Sinica*, Vol. 65, No. 4, pp. 1-7, Feb. 2016.
- [21] J. A. Ferreira, "Analytical computation of AC resistance of round and rectangular litz wire windings," *IEEE Proceedings B - Electric Power Applications*, Vol. 139, pp. 21-25, 1992.
- [22] Z. Yang, W. Liu, and E. Basham, "Inductor modeling in wireless links for implantable electronics," *IEEE Trans. Magn.*, Vol. 43, No. 10, pp. 3851-3860, Oct. 2007.



Ke-Han Zhang was born in Shaanxi, China, in 1971. He received his Ph.D. from Xi'an Jiaotong University, Xi'an China, in 2000 and his B.S. and M.S. degrees from Northwestern Polytechnical University. Currently, he serves as an associate professor and a master instructor in Northwestern Polytechnical university. His research interests focus on DSP-based brushless DC motor control system and wireless power transfer.



Zheng-Biao Zhu was born in Hunan in 1990. He received his B.S. degree from the School of Marine Science and Technology at Northwestern Polytechnical University, Xi'an, China, in 2015. He is currently a postgraduate in the School of Marine Science and Technology at Northwestern Polytechnical University, Xi'an, China. His current research interest is underwater wireless power transfer.



Luo-Na Du was born in Hubei, China in 1992. She received her B.S. degree from the School of Marine Science and Technology at Northwestern Polytechnical University, Xi'an, China, in 2015. Currently, she is pursuing her M.S. degree in the School of Marine Science and Technology at Northwestern Polytechnical University, Xi'an, China. Her main research interest is wireless power transfer technology.



Bao-Wei Song was born in 1963 in China. He is a professor and a doctoral tutor. He now serves as the Vice-Chancellor of Northwestern Polytechnic University. His current research interests include general technical research on underwater vehicles.